Chapter 5: Multifunctional Self-Assembled Hybrid of $CsPbCl_{1.5}Br_{1.5}$ with Terbium/Europium Metal-Organic Framework

5.1 Introduction

Metal-organic frameworks (MOFs) have garnered significant attention due to their wide range of applications such as sensing, LEDs, storage, optical anti-counterfeiting, etc.[192]. The porous nature of MOFs allows for the uniform intercalation of gas or metal molecules or ions within their structure. In Chapter 4, optical properties of the $CsPbBr_3$ interfaced Eu-MOF is discussed in detail. The $CsPbBr_3$ shows emission in the near green region and Eu-MOF in the red region. For the white light emitting diode (WLED) application, emision should be in the whole visible range (RGB: red, green and blue). In principle, this can be achieved easily by compositional mapping of halide ions in $CsPbX_3$ (X=Cl, Br, I) for blue emission and adding Tb^{3+}-ion for blue emiision with Eu^{3+}-ion in MOFs.

In this Chapter, we explored a single-phase $CsPbCl_{1.5}Br_{1.5}$@Tb/Eu-MOF for WLEDs application. In $CsPbCl_{1.5}Br_{1.5}$@Tb/Eu-MOF, the red component of the RGB spectrum is achieved by the Eu^{3+} ion, the green by the Tb^{3+} ion, and the blue by the characteristic broad emission of $CsPbCl_{1.5}Br_{1.5}$. The CIE color coordinates of the $CsPbCl_{1.5}Br_{1.5}$@Tb/Eu-MOF photoluminescence emission are calculated which is close to the standard white light CIE coordinates (0.333, 0.333). Further, in view of wavelength dependent color tunable emission of this material, the optical encryption and decryption application of this material is also explored. The encrypted patterns show color change under different wavelengths light illumination and thus can be used for strategic anti-counterfeiting application.

5.2 Synthesis Procedure

5.2.1 Synthesis of Tb/Eu-MOF

The Tb/Eu-MOF have been synthesized with Tb/Eu molar ratio 1:1, 4:1, and 9:1. For the synthesis of Tb/Eu-MOF with Tb/Eu molar ratio 1:1, equimolar amount of $Eu(NO_3)_3$ and $Tb(NO_3)_3$, 0.125 mmol of Eu_2O_3 (99.99%, Alfa Aesar) and 0.125 mmol of Tb_2O_3 (99.99%, Alfa Aesar) are taken separately in two beakers and required amount of HNO_3 (Qualigens, 5 ppm) is added into both. The solution is magnetically stirred at 200 rpm for 1 h at temperature 40 ºC to obtained clear transparent nitrate solution. Then temperature is increased to 120 ºC to remove the excess HNO_3 and H_2O from both the solutions. Then 5 mL dimethyle sulfoxide (DMF, 99%, EMPCURA) solution is added and magnetically stirred to obtain a clear transparent solution. In another beaker 0.5 mmol of 1,3,5 Benzene-tricarboxylic acid (H_3BTC, 98%, Thermo Scientific) is added into 15 mL of DMF, and magnetically stirred at 40 ºC for 1 h at 200 rpm to get perfectly dissolved solution. Then the DMF solution of $Eu(NO_3)_3$, $Tb(NO_3)_3$ and H_3BTC are mixed in a beaker and is ultra-sonicated for 10 minutes for uniform mixing. The homogeneous solution is transferred to a Teflon-lined autoclave and kept in a heating furnace at 125 ºC for 48 h for the coordination of the Ln^{3+} ion with the organic linker to form Tb/Eu-MOF. Then it is centrifuged at 7000 rpm and washed several times using ethanol. Precipitate is discarded and Tb/Eu-MOF (named a-Tb/Eu-MOF) particles are dried in a vacuum oven at 80 ºC for 12 h for further characterization. Similar steps are followed for the synthesis of 4:1, and 9:1 sample by taking required molar amount of Tb_2O_3 and Eu_2O_3.

5.2.2 Synthesis of $CsPbCl_{1.5}Br_{1.5}$@ Tb/Eu-MOF

The synthesis steps of $Pb(Cl/Br)_2$@Tb/Eu-MOF is same as that of Tb/Eu-MOF. $Eu(NO_3)_3$, $Tb(NO_3)_3$ and H_3BTC solutions are obtained as discussed above. For $CsPbCl_{1.5}Br_{1.5}$@Tb/Eu-MOF of Tb/Eu molar ratio 1:1, 0.05 mmol (0.0184 g) $PbBr_2$ (99.998%, Alfa Aesar) is dissolved in 0.5 mL HBr and 5 mL DMF solutions. Similarly, 0.05 mmol (0.0139 g) $PbCl_2$ (99.998%, Alfa Aesar) is dissolved in 0.5 mL HCl and 5 mL dimethyle sulfoxide (DMSO, 99%, EMPCURA) solutions. Subsequent procedures are same as discussed above. The obtained $Pb(Cl/Br)_2$@Tb/Eu-MOF particles after centrifugation are dried in a vacuum oven for 12 h at 80 ºC. Then, 0.05 mmol (0.0105 g) of CsBr (99.999%, Alfa Aesar) is dissolved in 4 mL of methanol (MeOH, 99%, Qualigens) and 1 mL of deionized (DI) water at 40 ºC for 30 min. Same step is followed for dissolving 0.05 mmol (0.0084 g) of CsCl (99.999%, Alfa Aesar). Then, CsBr and CsCl solution were mixed in a beaker and ultra-sonicated. The obtained $Pb(Cl/Br)_2$@ Tb/Eu-MOF power is mixed in a beaker containing mixed solution of CsBr and CsCl. Solution color changes from colorless to yellowish color, which is the indication of the formation of $CsPbCl_{1.5}Br_{1.5}$. It is magnetically stirred for the 10 min at 40 ºC with 200 rpm for uniform mixing to get the $CsPbCl_{1.5}Br_{1.5}$@Tb/Eu-MOF. Then it is centrifuged at 7000 rpm and washed several times using EOH. Precipitate is discarded and particles are dried in a vacuum oven at 80 ºC for 12 h. Finally, obtained yellowish color $CsPbCl_{1.5}Br_{1.5}$@Tb/Eu-MOF (a-CPCB@Tb/Eu-MOF) powder is used for the further characterizations and analysis.

For the synthesis of 4:1 Tb/Eu molar ratio's $CsPbCl_{1.5}Br_{1.5}$@Tb/Eu-MOF (b-CPCB@Tb/Eu-MOF), respectively, 0.25 mmol of $PbBr_2$, $PbCl_2$, CsBr and CsCl are used.

Similarly, for Tb/Eu 9:1 molar ratio's $CsPbCl_{1.5}Br_{1.5}$@Tb/Eu-MOF (c-CPCB@Tb/Eu-MOF), 0.5 mmol of $PbBr_2$, $PbCl_2$, CsBr and CsCl are taken.

5.3 Results and Discussions

5.3.1 Structure, Phase, Morphology, and Porosity analysis

X-ray diffraction (XRD) patterns were captured using nickel-filtered Cu-Kα (1.54 Å) radiation in a Miniflex 600 diffractometer from Rigaku, Japan. The 2θ range was from 10-90^0 and the step size was 0.02º. Phase purity of the synthesized a-Tb/Eu-MOF and $CsPbCl_{1.5}Br_{1.5}$ encapsulated a-Tb/Eu-MOF are studied through the XRD analysis. The XRD patterns of both the samples are shown in Fig. 5.1. Both have tetragonal phase, with space group $P4_322$, and is matched well with the earlier reported XRD data for the Tb-MOF and well as Eu-MOF [82]. Since XRD pattern of Tb/Eu-MOF is same as the XRD patterns of Tb-MOF and Eu-MOF, this confirms that the Tb/Eu atoms are well-coordinated with the organic-linker H_3BTC in the framing network. In this network each carboxylate group coordinates two Tb^{3+}/Eu^{3+}-ions and each ligand coordinates six Tb^{3+}/Eu^{3+}-ions through the oxygen atoms of the carboxylate. In Tb/Eu-MOFs network, luminescent guest $CsPbCl_{1.5}Br_{1.5}$ is encapsulated (a-CPCB@Tb/Eu-MOF). It is observed that the XRD positions of the a-CPCB@Tb/Eu-MOF retains as that of a-Tb/Eu-MOF. Although, change in intensity distribution of the diffraction peaks is observed. Changes in the preferred orientation of grains (texture) due to stress or strain can alter the intensities of the XRD peaks. If the grains reorient in a specific direction, the intensities of the corresponding peaks may increase while others may decrease.

To determine the lattice parameters of the a-Tb/Eu-MOF and a-CPCB@Tb/Eu-MOF, Lebail fitting have been done using "FullProf suite" software [193]. While fitting the

parameters, peak shape function selected is Pseudo-Voigt, and background mode is linear interpolation between set background points with refinable heights. Refinement weighting model is the Least Square. All the diffraction peaks are well indexed by the Bragg position of the tetragonal phase, with space group $P4_322$. Lattice parameters obtained for both the sample is listed in Table 5.1.

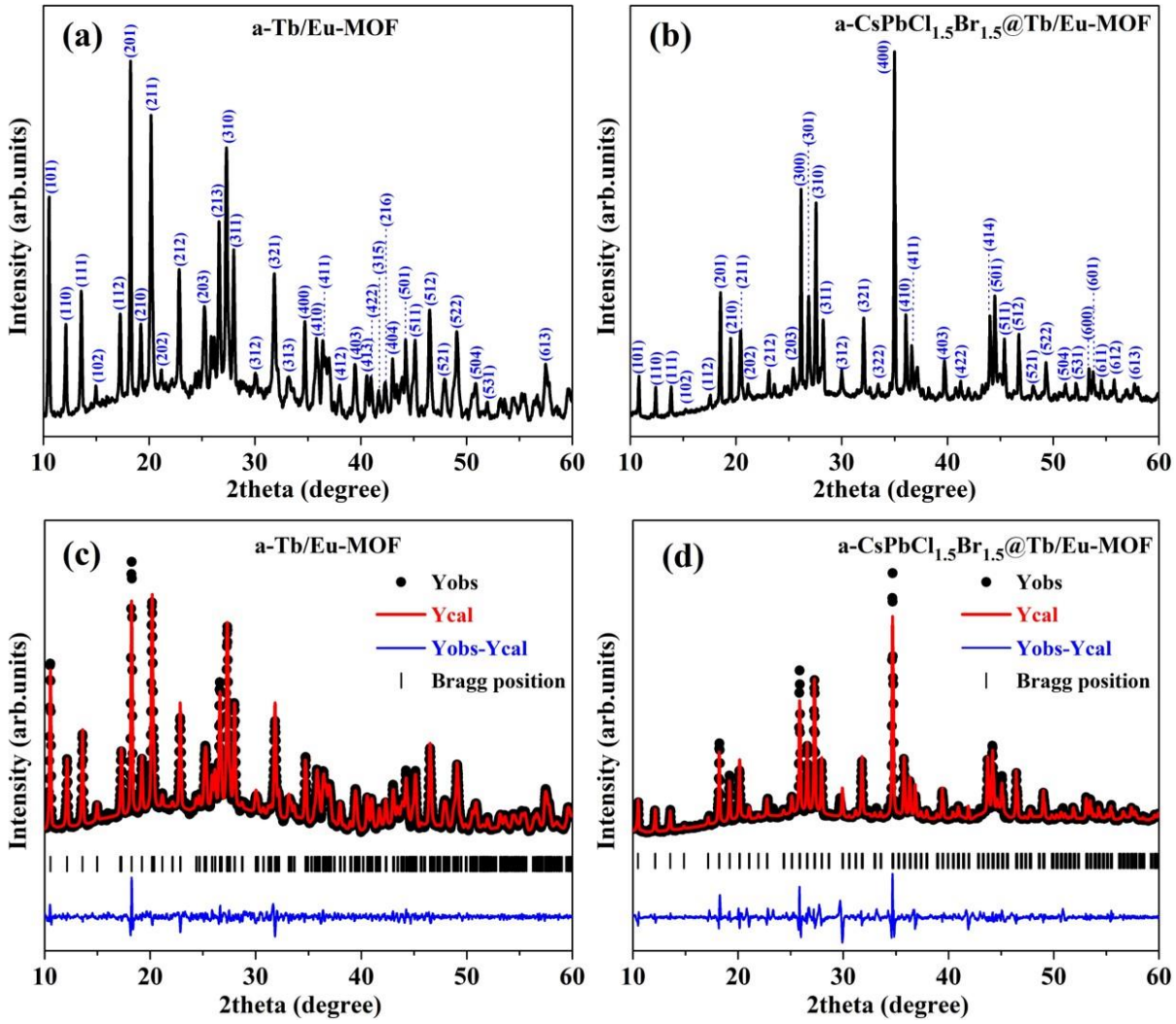

Figure 5.1: XRD patterns of as synthesized- (a) a-Tb/Eu-MOF, and (b) a-CPCB@Tb/Eu-MOF. Le-Bail fitted XRD patterns of (c) a-Tb/Eu-MOF, and (d) a-CPCB@Tb/Eu-MOF.

Sample a-Tb/Eu-MOF has $a = b = 10.33389 \pm 0.00017$ Å, and $c = 14.44475 \pm 0.00044$ Å. These parameters slightly get increased in a-CPCB@Tb/Eu-MOF and are $a = b = 10.34609$

$\pm$ 0.00020 Å and c = 14.61673 $\pm$ 0.00046 Å. These may be due to the strain induced in the organic chain of the linker molecule after the insertion of the CPCB into the Tb/Eu-MOF. Crystallite size is calculated using Debye Scherrer equation [109];

$$D = \frac{K\lambda}{\beta cos\theta} \quad \ldots (5.1)$$

Where K is the Scherrer constant (0.98), λ is the wavelength of the X-ray radiation, β is the full width at half maximum (FWHM) of the diffraction peak, and θ is the diffraction angle. Crystallite size of the a-Tb/Eu-MOF is 54 nm and it get increased to 63nm in a-CPCB@Tb/Eu-MOF. Large crystallite size tends to sharp diffraction peaks.

Table 5.1 Lattice parameters of the a-Tb/Eu-MOF and a-CPCB@Tb/Eu-MOF obtained by Le-Bail fitting.

Parameter	**a-Tb/Eu-MOF**	**a-CPCB@Tb/Eu-MOF**
Phase	Tetragonal	Tetragonal
Space group	$P4_322$	$P4_322$
$\boldsymbol{a = b}$ **(Å)**	10.33389 $\pm$ 0.00017	10.34609 $\pm$ 0.00020
$\boldsymbol{c}$ **(Å)**	14.44475 $\pm$ 0.00044	14.61673 $\pm$ 0.00046
$\boldsymbol{\alpha = \beta = \gamma}$ **(°)**	90	90
Volume (Å^3)	1542.544 $\pm$ 0.059	1564.599 $\pm$ 0.066
Godness of fit (χ^2)	2.66	3.95
Profile residual (*R*p)	7.28	4.43
Weighted profile residual (*R*wp)	10.8	7.29
Expected profile residual (*R*exp)	6.64	3.66

To get high-resolution pictures of synthesized MOF, EVO - Scanning Electron Microscope (SEM, MA15/18, Carl Zeiss Microscopy Ltd.) was used. Synthesized Tb/Eu-MOF's morphology is a bi-directional square needle, as shown in Fig. 5.2(a) - (c). Particle dimension and scaling are done through the "ImageJ" software. The needles' length is

between 15 to 60 μm, with an average length of 35 μm, and the angle of the needles lies between 7 – 9°. However, most bi-directional square needle lengths are between 20 to 40 μm. The distribution of the length of the bi-directional square needle is shown in Fig. 5.2(d). The bi-directional square needle middle thickness is ranging between 1.5–3.0 μm. Whereas, the tip of the bi-directional needle is about 300 nm. The SEM image showed that the needle formation occurs layer by layer and in both the directions. Before reaching the growth limit (we can term it the infant stage), it has a curved tip with a side slant-edge indicated in Fig. 5.2(b). At the limiting stage, it has a sharp, well-defined pyramidal tip, which is seen in the larger needle, as shown in Fig. 5.2(c). However, growth limit in terms of needle length is unclear by the SEM images. The curved tip with a side slant edge transformed into a sharp tip after crossing the infant stage, as observed in almost all bigger needles. At the same time, observing the infant needle, it was expected that the pyramidal-layer growth of the MOF progresses with the inner cell first and then the outer layer (seen Fig. 5.2(b)). However, it requires more insight into the reaction and mechanism to control the dimensions of the bi-directional square needle, such as length, thickness, sharpness, etc. The morphology of the a-CPCB@Tb/Eu-MOF is shown in Fig. 5.2(e). The morphology remains the same as a-Tb/Eu-MOF; however, needle length increases many times compared to the Tb/Eu-MOF. Elemental analysis has been done by energy dispersive spectroscopy (EDS) setup (model no. 51N1000, Oxford Instruments Nanoanalysis) equipped with the SEM. The EDX spectrum shows the presence of all the constituent elements i.e., Cs, Pb, Cl, Br, Eu, and Tb of the a-CPCB@Tb/Eu-MOF shown in Fig. 5.2(e).

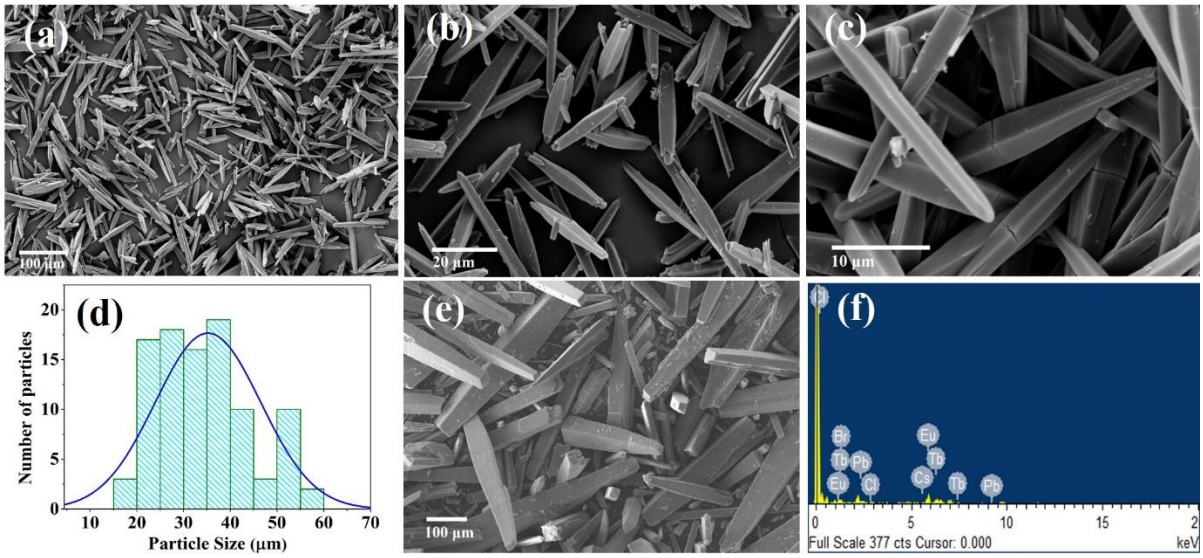

Figure 5.2: (a), (b), (c) SEM images of a-Tb/Eu-MOFs at different scale bar. (d) The a-Tb/Eu-MOFs bi-directional square needle's length distribution. (e) SEM image of a-CPCB@ Tb/Eu-MOFs. (f) EDX spectrum of a-CPCB@ Tb/Eu-MOFs.

The pore size of the MOF is estimated using the Brunauer–Emmett–Teller (BET) method using BELLSORP MAX II & BELCAT-II, MicrotracBEL setup. In order to measure the porosity, N_2 adsorption-desorption isotherm of a-Tb/Eu-MOF at 77 K is plotted, as shown in Fig. 5.3(a). The detailed description of the measurement technique is given in chapter 2. The relative pressure (P/P_0) upto 0.9, the N_2 adsorption phenomenon on the inner surface of the pore is obsereved. Beyond this pressure condensation takes places, as indiaceted by the abrupt rise of the isotherm curve, as shown in Fig. 5.3(a). There is no hysteresis in the isothermal i.e., desorption curve almost follows the adsorption cure. The pore size distribution is shown in the inset of Fig. 5.3(a). The BET analysis depicts that the average diameter of the pore is 4.22 nm, and total pore volume 54.717×10^4 μm^2 g^{-1}. This gives BET surface area of 1.0272 m^2g^{-1} (BET plot is shown in Fig. 5.3(b)). The mesoporous Tb/Eu-MOF has almost zero adsorption/desorption hysteresis (see Fig. 5.3(a)). The adsorbed N_2 molecules easility get released during desorption, hence this material can be highly suitable for gas sensing applications as well.

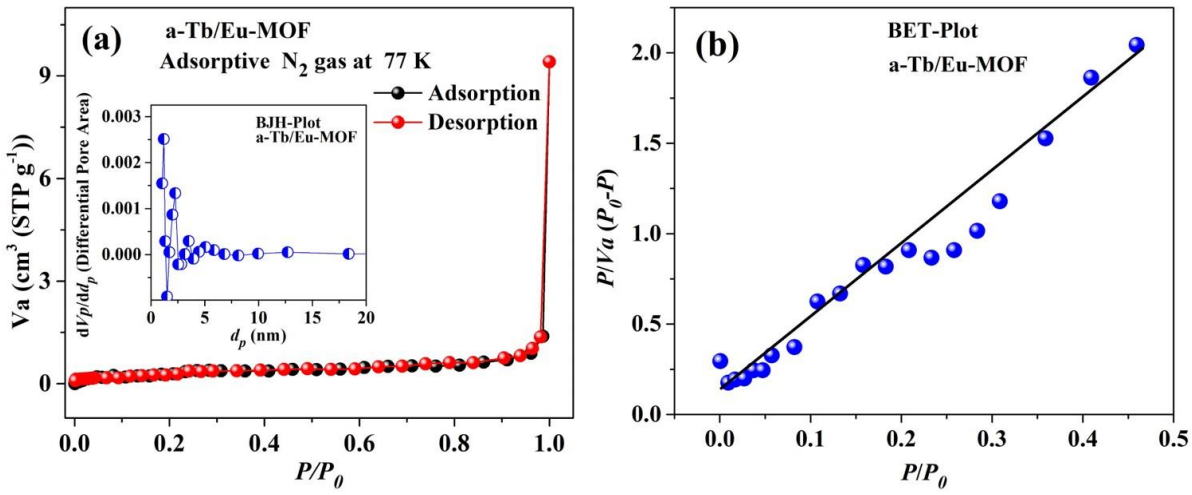

Figure 5.3: (a) N_2 adsorption/desorption plot of a-Tb/Eu-MOF. The inset shows the BJH plot of the pore size distribution, (b) BET plot of a-Tb/Eu-MOF.

5.3.2 UV-visible-NIR absorption analysis

UV-Vis-NIR absorption spectra, in the range from 250 nm–1200 nm, were recorded using the UV-2600 spectrophotometer (Shimadzu, Japan). UV-visible spectra of a-Tb/Eu-MOF and a-CPCB@Tb/Eu-MOF are shown in Fig. 5.4(a). In all the spectra, absorption below 350 nm is because of the organic linker H_3BTC. In addition, the Ln^{3+} characteristic absorption peaks were observed at 378, 395, 415, 464, 488, 535, and 591 nm. Among these, the absorption peaks at 378, 488, and 543 nm are because of Tb^{3+}, whereas peaks at 395, 415, 464, and 591 nm are because of the Eu^{3+}-ion. The absorption peak at 378 nm corresponds to the $^7F_6 \rightarrow {}^5G_6$ transition and the peak at 488 nm corresponds to the $^7F_6 \rightarrow {}^5D_4$ transition of Tb^{3+}-ion. On the other hand, the peak at 395 nm is assigned to the absorption transition $^7F_0 \rightarrow {}^5L_6$, 415 nm to the $^7F_0 \rightarrow {}^5D_3$, 464 nm to the $^7F_0 \rightarrow {}^5D_2$ transition of Eu^{3+}-ion. In 552–544 nm range, two weak intensity absorption bands of Eu^{3+} also appears for the transition $^7F_{0,1} \rightarrow {}^5D_1$. The peak at 591 nm is the absorption transition $^7F_1 \rightarrow {}^5D_0$ of Eu^{3+}. These absorption peaks indicate the presence of Tb and Eu both in the MOF. Despite these absorption peaks, in a-CPCB@Tb/Eu-MOF a sharp absorption edge appears at 466 nm (see Fig. 5.4(a)). This is the

characteristic absorption of the $CsPbCl_{1.5}Br_{1.5}$ and is the indication of successful entercalation of the $CsPbCl_{1.5}Br_{1.5}$ inside the a-Tb/Eu-MOF.

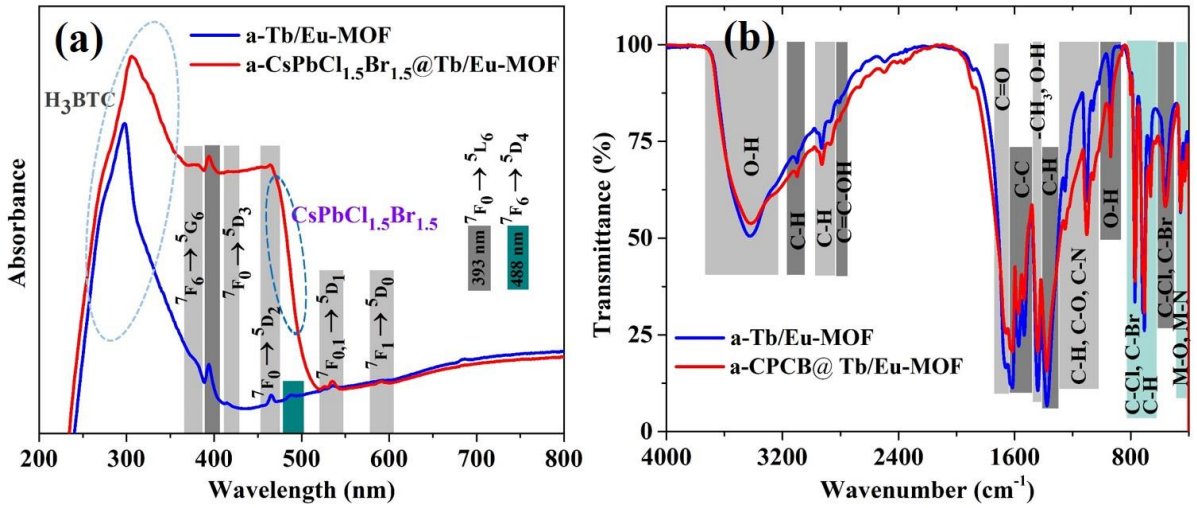

Figure 5.4: (a) UV-visible absorption spectra of a-Tb/Eu-MOF and a-CPCB@Tb/Eu-MOF. (b) FT-IR spectra of a-Tb/Eu-MOF and a-CPCB@Tb/Eu-MOF.

5.3.3 Fourier Transform-Infrared (FT-IR) analysis

The FT-IR spectra, in the range from 400–4000 cm^{-1}, were recorded using the Nicolet iS5 Thermofisher system. In the FT-IR spectra of the a-Tb/Eu-MOF and a-CPCB@Tb/Eu-MOF, as shown in Fig. 5.4(b), peaks appear at 3425, 3098, 2927, 2870, 2806, 1660, 1614, 1572, 1534, 1440, 1377, 1252, 1103, 1060, 938, 801, 771, 716, 705, 663, 562, 457, and 428 cm^{-1}. Among these, a broad peak centered at 3425 cm^{-1} is of the O – H stretching vibration of water molecules and alcohol [194]. A small peak centered 3098 cm^{-1} is of the = C – H stretching vibration of the H_3BTC aromatic ring. A peak at 2927 cm^{-1} arises due to the alkyl group's C – H stretching vibration. The C – H stretching vibration of alkane peaks at 2870 cm^{-1} [79][195]. The O = C – OH stretching vibration of carboxylate linked in the benzene ring of H_3BTC gives a peak at 2806 cm^{-1}. A peak at 1660 cm^{-1} represents the C = O stretching vibration of the carboxylate and amide in DMF [196]. In the FTIR spectra,

peaks centered at 1614, 1572, and 1534 cm^{-1} are contributed by C – C stretch in the aromatic ring of H_3BTC, and peaks at 1103 and 1060 cm^{-1} are due to C–H in-plane bending mode [195][196][197]. The O – H bending and – CH_3 waging are characterized by the 1440 cm^{-1} peak. This peak is also contributed by the stretching vibrations of carboxylate groups ($-COO^-$)[195]. On the other hand, peaks at 1103 and 1060 cm^{-1} are the characteristic peaks of the C – O stretch in alcohol. The 1377 cm^{-1} peak is assigned to the NO_3^- asymmetric vibration [197]. Alkyl halide's terminal C – H wag and carboxylic acid C – O stretching contribute to the 1252 cm^{-1} peak. The C – N stretching vibration of the DMF also contributes the peaks at 1252, 1103, 1060 and 1019 cm^{-1}. The O – H bending in carboxylic acid contributes to the peak at 938 cm^{-1}. The peaks between 515 to 850 cm^{-1} is contributed by the C – Cl and C – Br of the alkyl halide $–CH_2X$ (X=Cl, Br). The peaks in the range 675 to 900 cm^{-1} are also due to the aromatic ring's out-of-plane C – H bending [198]. At the same time, peaks at 771, 716, 705, 663, 562, 457, and 428 cm^{-1} may also be contributed due to the M – O (M=metal), M - N, M-X (X=Cl, Br) vibrations, etc[196][197][145]. This indicates the bonding of the Tb/Eu-metal with the organic linker and well as boning in CPCB. Hence, organic linker's hydrocarbons bond vibration as well as metal bonded with linker is assigned.

5.3.4 Photoluminescence (PL) study

5.3.4.1 PL excitation (PLE) spectrum

The c-CPCB@Tb/Eu-MOF is the optimized sample in terms of comparable PL emission intensity of all the three emitting centers i.e., Tb^{3+}, Eu^{3+}, and $CsPbCl_{1.5}Br_{1.5}$. PL spectrophotometer (Fluorolog-3, Horiba Jobin Yvon, USA) was employed to record the PL excitation and emission spectra. The PLE spectra of the c-CPCB@Tb/Eu-MOF is recorded for the prominent emission peak of Eu^{3+} ion (615 nm), as shown in Fig. 5.5(a), Tb^{3+} -ion

(489 and 543 nm) and for the luminescent guest center $CsPbCl_{1.5}Br_{1.5}$ (466 nm), as shown in Fig. 5.5(b). The excitation peaks are centered at 319, 352, 359, 362, 369, 376, 382, 393, 396, 415, 464, 486, 525, 534, and 589 nm for the 615 nm emission of Eu^{3+}[181]. Remarkably, among all these excitation peaks, the peak at 486 nm is the excitation transition of Tb^{3+}-ion ($^7F_6 \rightarrow {}^5D_4$) instead of Eu^{3+}. All these peaks (except 486 nm) arise from the transition of ground energy level $^7F_0$ to the different *J* values of the higher energy levels ^5D, ^5L, ^5G, and ^5H of Eu^{3+} -ion indicated in the energy level diagram shown in Fig. 5.6. In the UV region, the excitation peak centered at 352 nm for the transition $^7F_0 \rightarrow {}^5L_{10}$, 359 nm for the $^7F_0 \rightarrow {}^5L_9$, 362 nm for the $^7F_0 \rightarrow {}^5D_4$, 369 nm for $^7F_0 \rightarrow {}^5L_8$, 376 nm for the $^7F_0 \rightarrow {}^5G_2$, 382 nm for the $^7F_0 \rightarrow {}^5L_7$, 393 nm for the $^7F_0 \rightarrow {}^5L_6$, and the adjacent peak 396 nm for the $^7F_1 \rightarrow {}^5L_6$ in Eu^{3+} -ion. In the visible region, the excitation peaks at 415, and 464 nm are contributed by the transitions from the energy level $^7F_0$ to the $^5D_3$, and $^5D_2$ levels, respectively. The peaks at 525 nm and 534 nm arise, respectively, from the transition from $^7F_0$ and $^7F_1$, to the same higher-level $^5D_1$. The peak at 589 nm is ascribed to the transition $^7F_0 \rightarrow {}^5D_0$ in Eu^{3+}-ion. It is observed that the excitation spectrum recorded for the 615 nm emission peak consist of almost all the characteristic transitions of the Eu^{3+} -ion.

The excitation spectra of c-CPCB@Tb/Eu-MOF, recorded for the emission transition of Tb^{3+} occurring at 489 nm and 543 nm, shows a broad excitation band of H_3BTC between 250–320 nm, centered at ~295 nm which is attributed to the $\pi \rightarrow \pi^*$ electronic transition (see Fig. 5.5(b)). This band overlap with the spin-forbidden (ΔS=1) transition $4f^8 \rightarrow 4f^7 5d^1$ ($^7F_6 \rightarrow {}^9D$), and spin-allowed (ΔS=0) transition $4f^8 \rightarrow 4f^7 5d^1$ ($^7F_6 \rightarrow {}^7D$) of Tb^{3+}-ions, and the charge transfer band (CTB) of Eu^{3+}-O^{2-} ions [82]. Along with a broad charge transfer band peak at~ 298 nm, the peaks at 341, 351, 359, 369, 377, and 486 nm are also obsereved (see Fig.

5.5(b)). The 341 nm peak is the excitation transition from the ground energy level $^7F_6$ to $^5G_2$ in Tb^{3+}-ion. Similarly, 351, 359, 369, 377, and 486 nm excitation peaks are ascribed to the transition $^7F_6 \rightarrow {}^5D_2$, $^7F_6 \rightarrow {}^5L_9$, $^7F_6 \rightarrow {}^5G_5$, $^7F_6 \rightarrow {}^5D_3$, and $^7F_6 \rightarrow {}^5D_4$ of Tb^{3+}, respectively. Herein, we do not observe any excitation transition corresponding to Eu^{3+}.

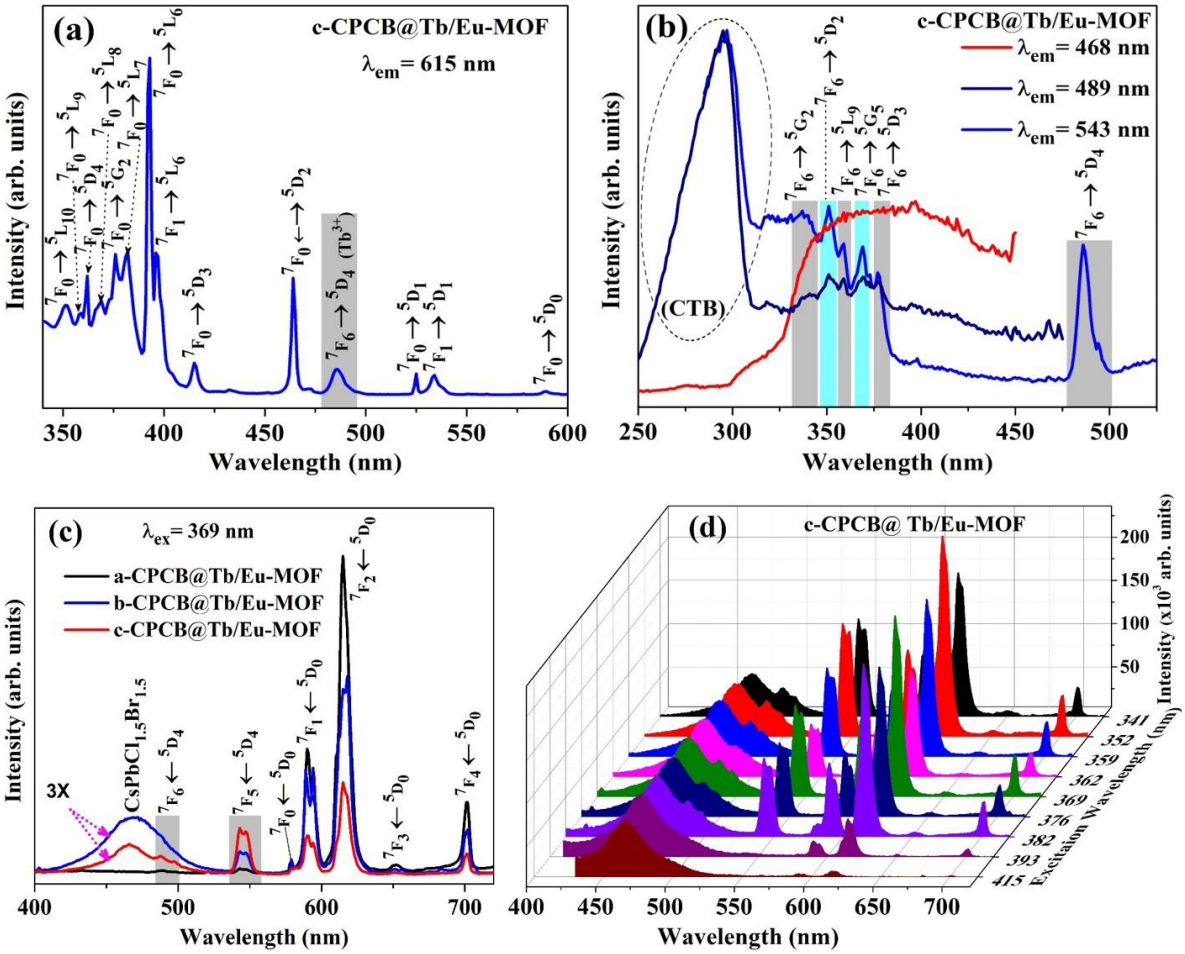

Figure 5.5: PLE spectrum of c-CPCB@ Eu/Tb-MOF monitored for the emission at (a) 615 nm of Eu^{3+}, (b) 489 nm, and 543 nm of Tb^{3+}, and 468 nm of CPCB. PL emission spectra of (c) a, b, c-CPCB@Tb/Eu-MOF excited by 369 nm. (d) PL emission spectra of c-CPCB@Tb/Eu-MOF under different excitation wavelengths in the wavelength range from 341 nm to 415 nm.

Further, the excitation spectrum was recorded for the 468 nm emission transition of guest-centered $CsPbCl_{1.5}Br_{1.5}$. The spectrum covers a broad region starting from 300 nm and falling beyond 400 nm, as shown in Fig. 5.5(b). Hence, several excitation transition of Tb^{3+}/Eu^{3+} overlap in the range of 300 nm to 400 nm. Therefore, the excitation of Tb^{3+}/Eu^{3+} in

this range also causes excitation to $CsPbCl_{1.5}Br_{1.5}$. Conclusively, the certain part of blue region (350 nm to 375 nm) can be used a common excitation wavelength for all the three emitters in CPCB@Tb/Eu-MOF showing the potential of this material for blue light excited WLEDs application.

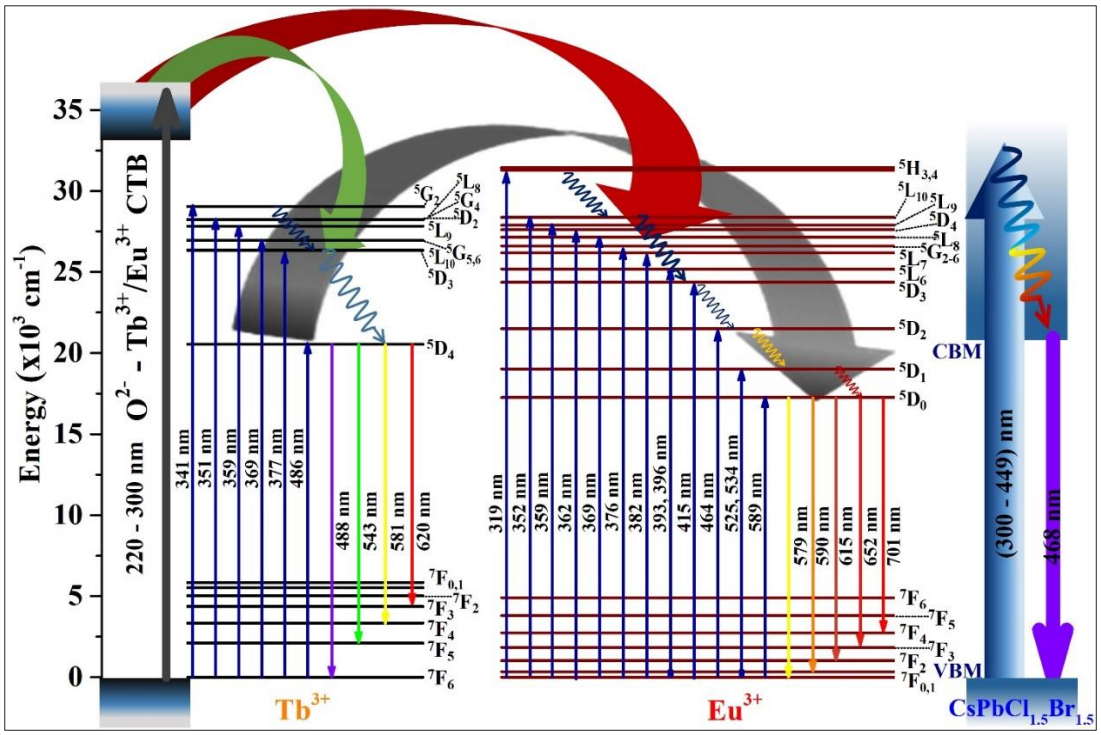

Figure 5.6: Energy level diagrams of Tb^{3+} and Eu^{3+}-ions (left panels), and energy band diagram of $CsPbCl_{1.5}Br_{1.5}$ (right panel), and energy transfer mechanisms among charge transfers band, Tb^{3+}, and Eu^{3+}-ions.

5.3.4.2 PL emission spectrum

In the luminescent guest-centered Ln-MOFs, PL emission is imparted by the guest-center and the Ln^{3+}-ions [184]. The excitation spectrum recorded for the emission peaks of Eu^{3+}, Tb^{3+} -ion, and $CsPbCl_{1.5}Br_{1.5}$ reveals that the many excitation bands of all the three emitting centers overlap in the 350–375 nm range. To see the relative PL emission intensity variation of the $CsPbCl_{1.5}Br_{1.5}$@ Tb/Eu-MOFs series, 369 nm excitation wavelength is chosen. The PL emission spectra of a-CPCB@Tb/Eu-MOF, b-CPCB@Tb/Eu-MOF, and c-CPCB@Tb/Eu-MOF are shown in Fig. 5.5(c). PL emission spectra consist of peaks centered

at 468, 488, 543, 579, 590, 615, 652, and 701 nm. The PL emission peak at 468 nm corresponds to the characteristic emission of luminescent guest $CsPbCl_{1.5}Br_{1.5}$. The peaks at 488 and 543 nm are assigned to the transitions $^5D_4 \rightarrow {}^7F_6$ and $^5D_4 \rightarrow {}^7F_5$, respectively, in Tb^{3+}-ion. Intensity of the other emission transition of Tb^{3+}-ion such as $^5D_4 \rightarrow {}^7F_4$ (581 nm) and $^5D_4 \rightarrow {}^7F_3$ (620 nm) are very week [82][83]. These low intensity peaks of Tb^{3+}-ion lie very close to the intense emission peak of Eu^{3+}-ion, hence, not noticeable in the PL emission spectrum. In the PL emission spectra, remaining peaks centered at 579, 590, 615, 652, and 701 nm arise due to transitions from the level $^5D_0$ to different *J* values of the level ^7F_J (0, 1, 2, 3, and 4) in Eu^{3+}-ion. 579 nm peaks is addressed by the transition $^5D_0 \rightarrow {}^7F_0$, 590 nm by the $^5D_0 \rightarrow {}^7F_1$, 615 nm by the $^5D_0 \rightarrow {}^7F_2$, 652 nm by the $^5D_0 \rightarrow {}^7F_3$, and 701 nm by the $^5D_0 \rightarrow {}^7F_4$ of Eu^{3+}-ion.

In CPCB@Tb/Eu-MOF samples series, the intensity of 615 nm peak of a-CPCB@Tb/Eu-MOF is ten times higher than the c-CPCB@Tb/Eu-MOF sample, and intensity of b-CPCB@Tb/Eu-MOF is two times higher than the c-CPCB@Tb/Eu-MOF sample. However, the intensity of the emission peak at 543 nm of Tb^{3+}-ion is the same for a-CPCB@Tb/Eu-MOF and b-CPCB@Tb/Eu-MOF, and the intensity of c-CPCB@Tb/Eu-MOF sample is two times higher than other two samples. On the other hand, the intensity of the emission peak corresponding to the guest $CsPbCl_{1.5}Br_{1.5}$ in b-CPCB@Tb/Eu-MOF is four times higher than the a-CPCB@Tb/Eu-MOF sample. Its intensity decreases in c-CPCB@Tb/Eu-MOF and is two times higher than the a-CPCB@Tb/Eu-MOF. The emission intensity of any particular emitting center in c-CPCB@Tb/Eu-MOF is comparably better than the a-CPCB@Tb/Eu-MOF and b-CPCB@Tb/Eu-MOF.

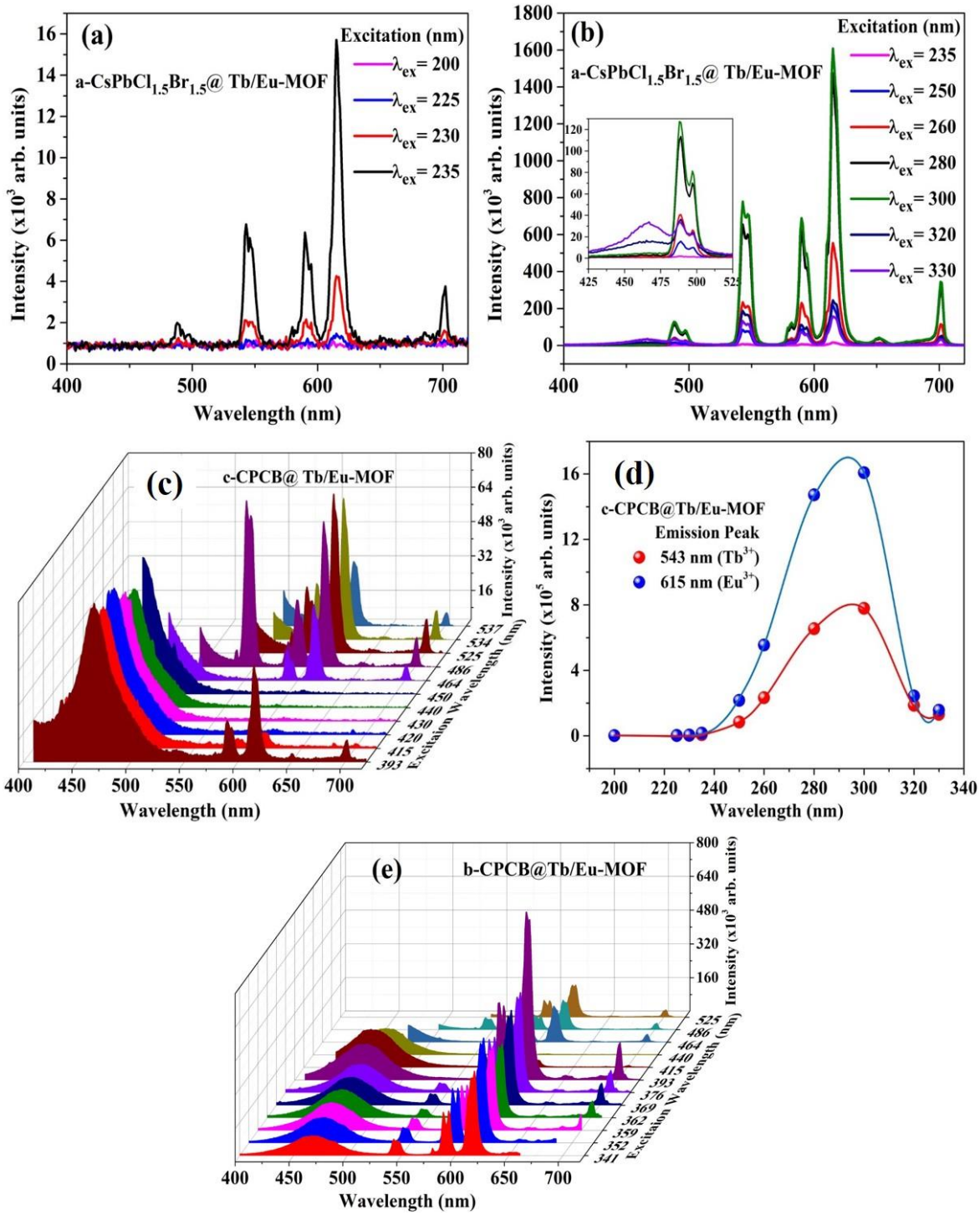

Figure 5.7: PL emission spectra of a-CPCB@ Tb/Eu-MOF in the excitation range (a) 200 – 235 nm, (b) 235 – 330 nm (c) 393 – 537 nm. (d) Variation of PL emission intensity of the 543 nm and 615 nm peaks of c-CPCB@Tb/Eu-MOF for different excitation wavelength in the range of 200-330 nm. (e) PL emission spectra of b-CPCB@ Tb/Eu-MOF in the excitation range 341 – 525 nm.

Further, to estimate the nature of CTB formed by Eu^{3+}/Tb^{3+}-ion with ligand and to understand the energy transfer mechanism among charge transfer band, Eu^{3+}/Tb^{3+}-ions, and $CsPbCl_{1.5}Br_{1.5}$, we have recorded the PL emission spectra of c-CPCB@Tb/Eu-MOF in the excitation range 200–530 nm. For 200 nm excitation, there is no emission in c-CPCB@Tb/Eu-MOF. At 225 nm excitation, a very weak 615 nm emission peak of Eu^{3+} is observed (see Fig. 5.7(a)). Further, as we move towards higher excitation wavelength, the intensity of the Eu^{3+}/Tb^{3+} emission peaks increases and the maximum is attained for 300 nm. Beyond this, the intensity of the PL emission peaks drops significantly, as seen for the 320 nm excitation.

The intensity of the 543 nm (Tb^{3+}) and 615 nm (Eu^{3+}) peaks are traced for these excitations. The intensity distribution profile is shown in Figure 5.7(d). From this observation, it is concluded that the CTB starts from 220 nm, peaking at ~295 nm, and ends at 320 nm. This is in fare agreement with the CTB shown in Fig. 5.5(b). The surprising result is that CTB does not excite the luminescent guest $CsPbCl_{1.5}Br_{1.5}$. The characteristic emission of $CsPbCl_{1.5}Br_{1.5}$ starts appearing in the emission spectrum beyond 300 nm excitation as it has a broad excitation band starting from 310 nm and extending well beyond 450 nm (see Fig. 5.7(b)). These results evidenced the fact that the charge transfer band of lanthanide-ions is ineffective for the guest center $CsPbCl_{1.5}Br_{1.5}$ emissions. Hence, $CsPbCl_{1.5}Br_{1.5}$ can only be activated by its own excitation band.

In the region 330–390 nm, most of the excitation bands of Tb^{3+} and Eu^{3+}-ion overlap. Hence, in the PL emission spectra, the contribution of both Tb^{3+} and Eu^{3+}-ions and $CsPbCl_{1.5}Br_{1.5}$ are present, as shown in Fig. 5.5(d). Between 415 – 464 nm, the excitation band of both Tb^{3+} and Eu^{3+}-ions is absent, therefore only $CsPbCl_{1.5}Br_{1.5}$ emission peak is

observed in the PL emission spectra (see Fig. 5.7(c)). There is a Tb^{3+}-ion's excitation band peak at 486 nm. This excitation band contributes to the emission transition for Tb^{3+} and Eu^{3+}-ions both. After this, only Eu^{3+}-ion's excitation bands are present, which contributes only to Eu^{3+}-ion's PL emission peaks in the spectra. The b-CPCB@Tb/Eu-MOF emission spectra also show the same trends of Tb^{3+} and Eu^{3+} ion emission transitions at different excitation wavelengths, as shown in Fig. 5.7(e).

***Conclusive remarks from PL analysis*:** First: CTB of Tb^{3+} and Eu^{3+}-ions is ineffective in exciting the luminescent guest center $CsPbCl_{1.5}Br_{1.5}$. However, CTB efficiently sensitizes the Tb^{3+} and Eu^{3+}-ions both. The luminescent guest $CsPbCl_{1.5}Br_{1.5}$ is sensitized only by its own excitation band, and is ineffective in sensitizing other two emission centers Tb^{3+} and Eu^{3+}-ions. Second: An energy transfer from Tb^{3+} to Eu^{3+} is observed which is evident by (i) the presence of excitation band of Tb^{3+} (486 nm) while excitation spectrum is recorded for the emission transition of Eu^{3+} (615 nm). (ii) When Tb is excited selectively with 486 nm in a-CPCB@Tb/Eu-MOF sample, the emission corresponding to Tb is almost negligible while emission of the Eu^{3+} is significantly observed. However, this energy transfer is unilateral, the excitation band corresponding to Eu^{3+} facilitates only its own emission transitions not to Tb^{3+}. (iii) The emission intensity of the green transition of Tb^{3+}-ion is very weak in a-CPCB@Tb/Eu-MOF and it is improved further in b-CPCB@Tb/Eu-MOF and c-CPCB@Tb/Eu-MOF sample, obiously because of a change in the molar ratios of Tb/Eu which increases the Tb content in the sample comparatively. Significantly, this variation in molar ratio of Tb/Eu optimizes the intensity ratio of green (of Tb^{3+}) and red (Eu^{3+}) emissions by the sample which leads to a color tunability and ultimately a white light emission, which

opens the scope of this material for different applications e.g. for WLEDs and anticounterfeiting.

5.4 Multifunctional Applications

5.4.1 White light emitting diode (WLED) application

The Commission Internationale de l'Eclairage (CIE) 1931 chromaticity diagram is a fundamental tool in color science research, aiding in studying human color perception and developing new color models and standards. Chromaticity coordinates on the CIE 1931 diagram are used to design and calibrate display devices (monitors, televisions, projectors) to ensure accurate color reproduction.

The selection of specific lighting at a particular place is crucial to concentrate the human and other minds towards the events. In WLEDs fabrication, correlated color temperature (CCT) is one of the most important parameters. WLEDs with CCT values between 2500 – 3500 K have a percentage of the red component, creating a warm sensation in the mind and referred to as warm light [199]. On the other hand, CCT values between 4500 – 6500 K are termed as cold light.

According to the CIE 1931, color coordinates (x, y) in the chromaticity diagram is (0.333, 0.333) for the white light. The CCT, CIE (x, y) coordinate, and CRI values for different Tb/Eu-MOFs previously reported for WLEDs application are listed in Table 5.2. In Tb/Eu-MOFs based WLEDs, Tb^{3+}-ion contributes green component, Eu^{3+}- ion contributes red component, and the blue part is either contributed by luminescent guest materials or linker-centered emission. Table 5.2 shows that the WLEDs parameters are affected by the organic ligands and luminescent guest significantly.

Table 5.2 Different linker used guest luminescent centers attached Eu/Tb-MOFs WLEDs photometric values.

Eu/Tb-MOFs	Organic ligand	CCT(K)	CIE (x, y)	CRI	Ref
$CsGeBr_3$@ Eu^{3+}		3020	(0.423, 0.379)	92	[200]
Eu^{3+}/Tb^{3+}	4,4′-(2-sulfostyryl) biphenyl disodium	5536	(0.34, 0.36)	86	[201]
Eu^{3+}/Tb^{3+}	terpyridine-based polymer	3347	(0.385, 0.324)	84	[202]
Eu^{3+}/Tb^{3+}	2,2′-bipyridine-5,5′-dicarboxylic acid	4914	(0.348, 0.329)	75	[203]
Eu^{3+}/Tb^{3+}	4-cyano-biphenyl-3-carboxylic acid	5562	(0.331, 0.328)	81.7	[204]
Eu^{3+}/Tb^{3+}@CDs	1,4-phenylenediacetic acid	5443	(0.334, 0.334)	93	[205]
Eu^{3+}/Tb^{3+}@Zn	3,5-bis(1-methoxy-3,5-benzene dicarboxylic acid) benzoic acid	-	(0.312, 0.335)	-	[206]
Eu^{3+}/Tb^{3+}@Ga	1,2,4-benzenetricarboxylic acid	-	(0.369, 0.336)	-	[207]
Eu^{3+}/Tb^{3+}@Zn	1,3,5-tri(4-carboxyphenoxy) benzene carboxylic acid	-	(0.329, 0.354)	-	[208]
Eu^{3+}/Tb^{3+}	4,4′-(((5-carboxy-1,3-phenylene) bis(oxy)) bis(methylene)) dibenzoic acid	5733	(0.326, 0.342)	73.4	[209]
Eu^{3+}/Tb^{3+}	4,4′-biphenyldicarboxylic acid	4725	(0.328, 0.338)	86.2	[210]
Eu^{3+}/Tb^{3+}@La	4,4',4''-nitrilotribenzoic acid	-	(0.319, 0.344)	-	[211]
Eu^{3+}/Tb^{3+}@ $CsPbCl_{1.5}Br_{1.5}$	1,3,5 Benzene-tricarboxylic acid	4392	(0.351, 0.298)	73	This work

In a-CPCB@Tb/Eu-MOF sample, the emission peak intensity of CPCB and Tb^{3+}-ion is insignificant compared to Eu^{3+}-ion. Whereas, in the samples b,c-CPCB@Tb/Eu-MOF all the three components emit proportionaly for WLED application, the red component of the RGB is achieved by the Eu^{3+}-ion, green from the Tb^{3+}-ion, and the blue color is imparted by the characteristic broad emission of $CsPbCl_{1.5}Br_{1.5}$. CIE 1931 diagram for the b-CPCB@Tb/Eu-MOF and c-CPCB@Tb/Eu-MOF are shown in Fig. 5.8(a) and 5.8(b), respectively. The CIE (x, y) coordinates of b-CPCB@Tb/Eu-MOF sample are (0.368, 0.247), (0.380, 0.252), and (0.385, 0.251) for the excitation 359, 369, and 376 nm, respectively. The CIE (x, y) coordinates of the c-CPCB@Tb/Eu-MOF have more proximities to standard white light coordinates than the b-CPCB@Tb/Eu-MOF. Among 352, 359, 369, 376, and 382 nm excitation wavelengths, 359 nm excitation gives the best CIE

(x,y) coordinate (0.351, 0.298) closer to standard white light coordinate than the other excitation.

The CCT value for the 359 nm excitation is 4392 K, aligned towards the cool white light. However, others values lie in the range 3400 – 4900 K. Visible light power output (Vis) quantifies the actual power of the light emitted within the visible spectrum. Under different wavelength excitation, the obtained value of Vis lies between 8500 and 1000 mW. It has efficient outpout power of the emitted light suitable for the lighling. Luminous Efficacy of Radiation (LER) measures how effectively the emitted light corresponds to the visible spectrum the human eye perceives. LER obtained for different excitation wavelengths lies in the 250-300 lm/W range suitable for lighting. Which is the acceptable range for the WLEDs. Color rendering index (CRI) is the parameter that gives the sensation of the color emitted by the object to the human eyes. The CRI value of the emitted white light under excitaion 352–382 nm range is below 100, acceptable for WLEDs.

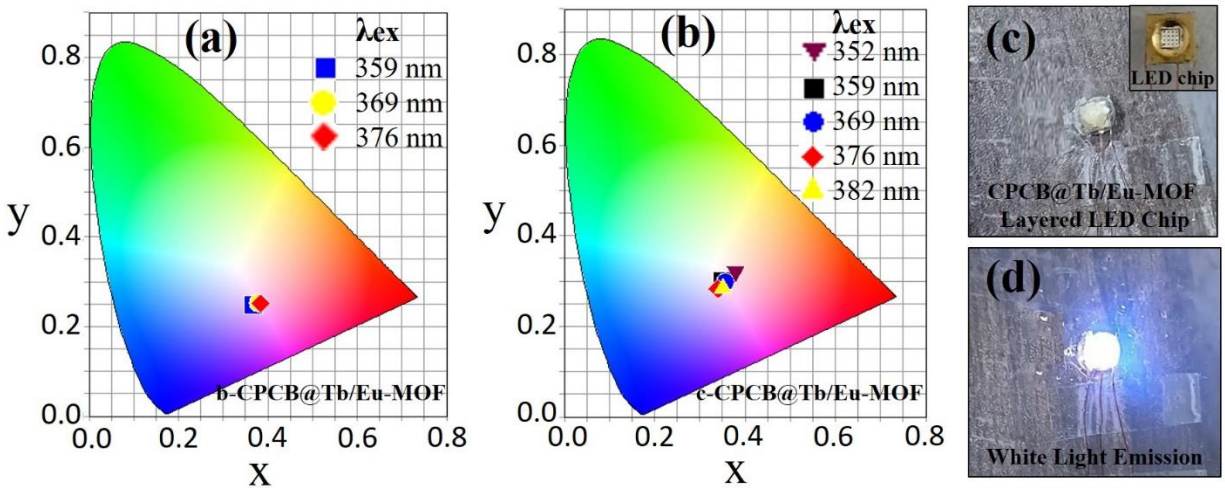

Figure 5.8: CIE 1931 coordinates of emission spectra of (a) b-CPCB@Tb/Eu-MOF, (b) c-CPCB@Tb/Eu-MOF at different excitation wavelengths. (c) The c-CPCB@Tb/Eu-MOF PMMA matrix coated UV-LED chip (inset: UV-LED chip) , and (d) white light emission under operation.

The CIE (x, y) coordinates, CCT, Vis, LER, and CRI values for the different excitation wavelengths are listed in Table 5.3. It is clear from the parametric study that tailoring the molar concentration of Tb, Eu and $CsPbCl_{1.5}Br_{1.5}$ in MOF can lead to perfect WLEDs.

Table 5.3 Photometric study of the c-CPCB@Tb/Eu-MOF for WLED.

Excitation Wavelength (nm)	CIE (x, y)	CCT (K)	Vis (mW)	LER	CRI
352	(0.380, 0.323)	3485	9687	277	77
359	(0.351, 0.298)	4392	8660	258	73
369	(0.357, 0.298)	4051	9364	257	71
376	(0.340, 0.283)	4892	8597	246	66
382	(0.351, 0.286)	4239	8983	250	66

To visualize the white light emission from the synthesizd c-CPCB@Tb/Eu-MOF, UV-LED chip (367 nm radiation) is employed. The c-CPCB@Tb/Eu-MOF is caped into poly(methyle methacrylate) (PMMA) matrix and then layered onto the radiating portion of UV-LED. It is vaccume dried for 24 h to remove moisture present in the matrix and perfectly fixing it on the LED chip (see Fig. 5.8(c)). It gives whitish emission, as shown in Fig. 5.8(d), when UV-LED chip is oprated at 3 volt power supply. Hence, this material can be a future WLED material for lighting applications.

5.4.2 Optical anti-counterfeiting application

From the PL study, it was observed that the wavelength-dependent selective excitation of the different luminescent centers in $CsPbCl_{1.5}Br_{1.5}$ @ Tb/Eu-MOF gives emission in different color. This changes CIE (x, y) coordinates and, hence different color sensations to the eyes. We have calculated the CIE (x, y) coordinates of both the samples i.e. b-CPCB @ Tb/Eu-MOF and c-CPCB @ Tb/Eu-MOF for selective excitation, as listed in Table 5.4. The c-CPCB @ Tb/Eu-MOF's CIE (x, y) coordinates distribution is large compared to b-CPCB @

Tb/Eu-MOF. The CIE 1931 (x, y) coordinate for both samples is shown in Fig. 5.9. The b-CPCB @ Tb/Eu-MOF color purity for 300 nm excitation is 93.8 %; for 420 nm, it is 81.3 %; and for 486 nm excitation, it is 94.6 %. On the other hand, c-CPCB @ Tb/Eu-MOF shows color purity for the 300 nm excitation is 92.4 %, for 420 nm it is 70.5 %, and for 486 nm excitation it is 94.8 %. So, one can distinguish the color appearance of the encrypted patterns under these excitation wavelengths very clearly.

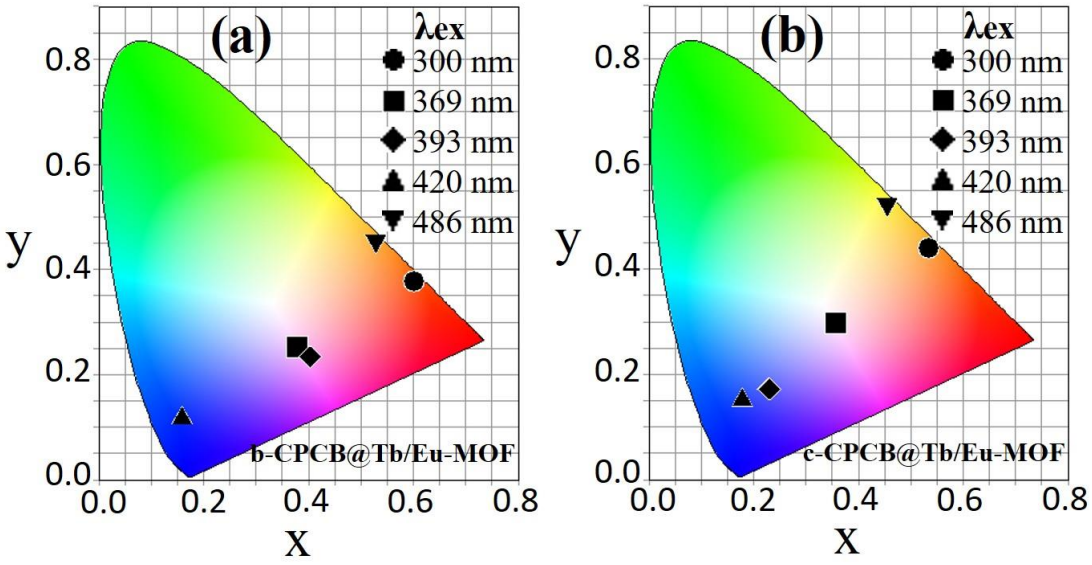

Figure 5.9: CIE 1931 plot of (a) b-CPCB @ Tb/Eu-MOF and b-CPCB @ Tb/Eu-MOF for excitation wavelengths 300, 369, 393, 420, and 486 nm.

Table 5.4 CIE (x, y) coordinate of $CsPbCl_{1.5}Br_{1.5}$ @ Tb/Eu-MOF under different excitation wavelengths.

Excitation Wavelength (nm)	**CIE (x, y) coordinate of $CsPbCl_{1.5}Br_{1.5}$ @ Tb/Eu-MOF**	
	b-CPCB@Tb/Eu-MOF	**c-CPCB@Tb/Eu-MOF**
300	(0.602, 0.376)	(0.535, 0.440)
369	(0.380, 0.252)	(0.358, 0.298)
393	(0.404, 0.234)	(0.231, 0.173)
420	(0.158, 0.118)	(0.179, 0.152)
486	(0.528, 0.456)	(0.455, 0.527)

On the basis of this idea, a letter "W" was coded by using c-CPCB @ Tb/Eu-MOF sample on different surfaces: borosilicate glass (W-BG), aluminum foil (W-AF), transparent plastic (W-TP), black paper (W-BP), and white paper (W-WP). Digital photographs of the color appearance of the developed code exposed under the light of wavelength 300, 369, 393, 420, and 486 nm are shown in Fig. 5.10. Under 300 nm light exposure, the encrypted pattern "W" glows in reddish-orange, while under 369 nm light, it appears nearly white. The pattern color is bluish-purple under 393 nm light, and its color appearance changes to blue under 420 nm. The pattern looks greenish-yellow under 486 nm light.

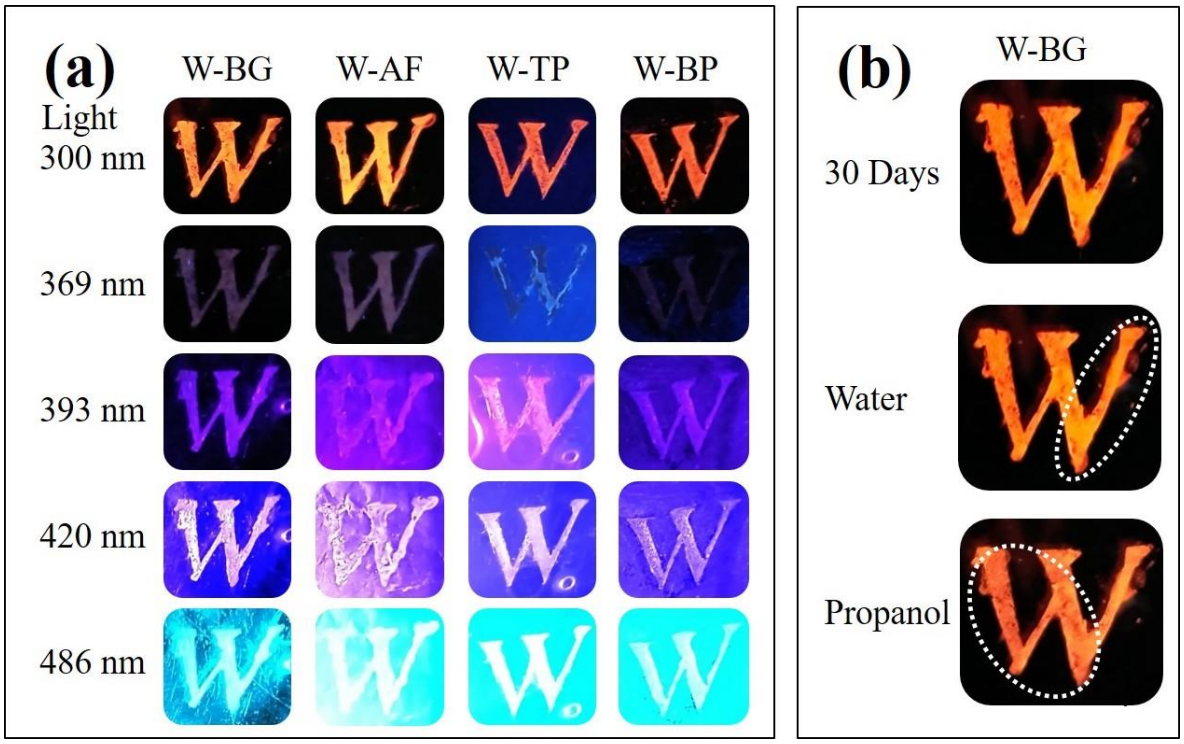

Figure 5.10: Digital photographs of the encrypted patterns taken under the exposure of different wavelength light illumination. (b) Stability of the pattern "W-BG" in an open environment, on water and propanol treatment (marked area).

Among the different surfaces used for the encryption of the pattern, "W-BG" and "W-BP" have the best appearance. Therefore, the chemical and physical stability and durability of the encrypted pattern "W-BG" is selected and tested under different chemical conditions,

such as water and propanol. Pattern color, observed under 300 nm after 30 days, appears the same as the digital photograph taken just after the encryption (see Fig. 5.10(a) and 5.10(b)). Water encounter to the pattern doesn't affect the pattern (see marked in Fig. 5.10(b)). The propanol solution slightly degrades the pattern's physical form, and the contrast of the digital photograph reduces slightly, as seen under 300 nm UV light.

Thus, $CsPbCl_{1.5}Br_{1.5}$@ Tb/Eu-MOF's encrypted "W" patterns show color change under different wavelengths of light illumination. The selected pattern, "W-BG" shows physical and chemical stability under water, ethanol, and in an open environment. Hence, this material can be one of the best single-structured and multi-color emissive material for multi-level anti-counterfeiting applications.

5.5 Conclusions

In conclusion, lead free inorganic halide perovskite ($CsPbCl_{1.5}Br_{1.5}$, CPCB) intercalated dual lanthanide based metal organic framework (Tb/Eu-MOFs) is synthesized, which forms bi-directional needle-like hybrid structures. The single tetragonal phase of Tb/Eu-MOFs and CPCB@Tb/Eu-MOF was verified by the LeBail fitting of the XRD data. Successful incorporation of the inorganic halide perovskite into Tb/Eu-MOF is evidenced by the characteristic absorption band and by the EDAX analysis. Optical studies show that there are three emitting centers in CPCB@Tb/Eu-MOF i.e. Eu^{3+}, Tb^{3+} and $CsPbCl_{1.5}Br_{1.5}$. Tb^{3+} and Eu^{3+}-ions are sensitized by their charge transfer bands and characteristic excitations. An energy transfer from Tb^{3+} to Eu^{3+} is is also observed which is evident by (i) the presence of excitation band of Tb^{3+} (486 nm) while excitation spectrum is recorded for the emission transition of Eu^{3+} (615 nm). (ii) When Tb is excited selectively with 486 nm in a-CPCB@Tb/Eu-MOF sample, the emission corresponding to Tb is almost negligible while

emission of the Eu^{3+} is significantly observed. However, this energy transfer is unilateral. On the other hand, $CsPbCl_{1.5}Br_{1.5}$ is sensitized only by its own excitation band, and optically inactive to Tb^{3+} and Eu^{3+}-ions. Significantly, a variation in the molar ratio of Tb/Eu optimizes the intensity ratio of green (of Tb^{3+}) and red (Eu^{3+}) emissions which leads to color tunability. The white light emission is achieved by exciting the sample in the range from 341 nm to 382 nm. The best CIE coordinate (0.357, 0.298) tending to white light is achieved for 369 nm excitation. Different parametrs calculated for the white light (e.g. CCT, CRI, vis, and color purity, etc.) suggest that it is a cool white light with excellent rendering index. Further, the excitation wavelength-dependent emission spectrum spans from blue to yellowish-red region with the maximum color purity (CP) of 94.8%, highlighting the potential of material for anti-counterfeiting application as well. In this line, the letter "W" based code was encrypted on four different substrates which exhibit significant color change under different excitation wavelengths. The stability test of the encrypted codes show that the code developed on borosilicate glass is the most stable over time in ambient conditions and under various chemical exposures. In conclusion, CPCB@Tb/Eu-MOF hybrid is a multifunctional material suitable for white light emission, and for encryption-decryption.